J Mater Sci (2006) 41:6737–6750
DOI 10.1007/s10853-006-0212-7

# Bridging the length-scale gap—short fibre composite material as an example

**R. Pyrz · J. Schjødt-Thomsen**

Published online: 12 August 2006


**Abstract** A sequential modelling approach consisting of passing information across length scales is presented to simulate macroscopic behavior of composite materials. The modeling procedure utilizes a proper flow of information from molecular scale to macroscopic scale including material characteristics at different length scales. Both molecular dynamics and analytical/numerical methods were used in the multiscale analysis together with some experimental observations obtained from Raman microspectroscopy and X-ray microtomography. The multiscale procedure is systematically applied to short glass fibre polypropylene composite material.

## Introduction

The concept of length scales exists because of the classes of physical theories and models that have been developed to describe material behaviour. Boundaries between the length scales are delineated by the breakdown in the assumptions implicit to a particular scale. Thus we can define each scale by the phenomena that are treated discretely and the phenomena that are treated collectively. The two exceptions are the end points of the length scales. Everything at the electronic scale is treated discretely whereas everything at the macro scale is treated collectively. This concept is illustrated in Fig. 1. Starting the description from the smallest scale i.e. going in the direction opposite to the length scale arrow, the atoms and molecules are treated discretely at the atomic scale and the electrons are treated collectively. At the micro scale the atoms forming crystals are treated collectively and the interface between composite matrix material and the fibre reinforcement is treated discretely. At the next scale level interfaces are treated collectively and single fibres are treated discretely. At the continuum level the microstructure (such as representative volume element) is treated discretely while the microstructure descriptors (such as fibre orientation, volume fraction, length distribution etc.) are treated collectively. Finally, the macro scale represents a collection of continuum treatments, i.e. structural application.

Modelling and simulation are becoming increasingly ambitious. On the one hand, there are calculations, which aim at increasingly precise and detailed description. A number of assumptions is minimized, and empirical elements are replaced wherever possible. The improvements in detail yield improvements in accuracy, and provide the potential tool to resolve previously intractable problems. On the other hand, increasingly large systems are being investigated. These have different challenges. The methods, which are best for studies concentrating on a few atoms, may be inefficient for larger structures; there may be more alternative structures possible than are obvious from the smaller scale systems and, finally, the interpretation itself may be difficult without other aids. There is therefore a need to link experience at the macroscopic level with the understanding from an atomic scale. Another area of growing significance is that of the analysis of microstructural evolution. The architecture of materials microstructure changes depending on synthesis and manufacturing conditions resulting in different morphological configurations of constituents. Once the relevant geometrical and physical structures have been identified for a given synthesis and production route, it is possible to turn to modelling and simulation of the properties that they imply, Fig. 2. This

R. Pyrz (✉) · J. Schjødt-Thomsen
Institute of Mechanical Engineering, Aalborg University,
Pontoppidanstraede 101, 9220 Aalborg East, Denmark
e-mail: rp@ime.aau.dk

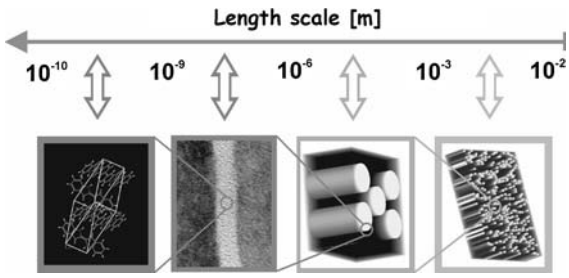


**Fig. 1** Physical length scales

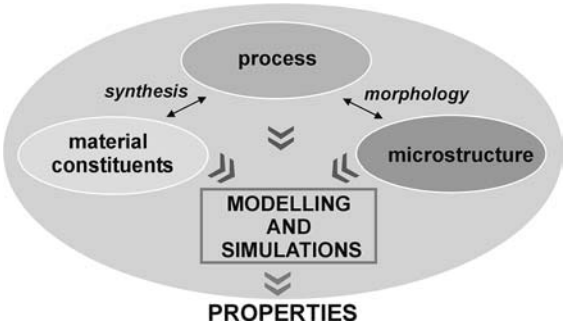


**Fig. 2** Flow chart relating materials structure to properties

flow chart is valid for any selected length scale differing only in a degree of details incorporated in the analysis.

In principle, all length scales are covered by two fundamental physical models: discrete atomic models and continuum field theories. In the range of several nanometres and below, we are dealing with collections of discrete particles interacting in terms of multi-body potentials. The atomic-scale calculations allow examining many processes that remain otherwise experimentally inaccessible. On the other hand, continuum mechanics describes a material system in terms of macroscopic variables such as mass, stress and strain that significantly enlarges the applicability region and facilitates direct measurements possibilities. The integration of both methods has resulted in a number of approaches, which combine discrete atomistic simulations with continuum field theories and finite element methods. The equivalence of the continuum to discrete atomic system has been derived in a framework of micromorphic theory [1–3] and non-local elasticity [4]. The atomic-scale finite element method [5] and quasicontinuum method [6–8] combine atomically derived information and the discretization of an object by finite elements. Coarse-grained and projection approaches are presented in [9, 10] that link atomic and continuum level.

The effective properties of multi-phase materials can be determined through a homogenization technique in which the heterogeneous medium is replaced by a homogeneous one with anisotropic properties, which have to be determined. This kind of analysis provides overall behaviour of a material from the known properties of the individual constituents, their interaction, shape, orientation and volume fraction [11, 12].

However, the behaviour of short fibre reinforced composites is not only a function of the aforementioned quantities, but also of the interfacial bonding quality, which governs a majority of mechanical properties of the composite. The mechanical properties of a composite depend critically on the load transfer efficiency at the interface between fibre and matrix material. For carbon fibre reinforced composites with non-reactive matrices, such as semicrystalline thermoplastic polymers, the adhesion is primarily a result of mechanical interaction. Thermoplastics undergo large volume changes during crystallization in addition to the differential thermal expansion between the fibre and matrix. This will impose a compressive stress on the fibre and increase the load transfer efficiency. However, the level of residual stresses is dependent on the cooling rate due to viscoelasticity and crystallization behaviour of the matrix. For semicrystalline polymers like polypropylene, heterogeneous nucleation on the fibre surface may affect residual stresses. If the nucleation density is sufficiently high the spherulites impinge and can grow only in one direction, normal to the surface of the fibre, developing a transcrystalline interphase. The transcrystalline interphase is often large in diameter compared to the fibre and for a practical composite having a large volume fraction of fibres the bulk matrix may predominantly have a transcrystalline morphology. Due to the nucleation on the fibre surface and the anisotropy of this phase, the transcrystalline interphase may be expected to affect the properties of the composite by influencing thermal residual stresses and the mechanical properties of the surrounding matrix. Thus the fundamental tasks in the prediction of the overall mechanical properties are to determine parameters describing crystallization kinetics, thermorheological behaviour of the matrix and properties of the interphase being formed between the fibre and the solidifying matrix.

In this paper, several aspects of multiscale modelling of short fibre composites at different length scales are presented.

## Molecular level

In melt-crystallized polymers, such as polypropylene, the morphology is usually lamellar consisting of stacks of crystallites separated by the amorphous phase, Fig. 3. Model composites with a transcrystalline interlayer were manufactured by embedding single carbon fibres (unsized PAN based high modulus) between isotactic-polypropylene films [13]. The assembly was heated to melt (205 °C) for 5 min under a light pressure to exclude air and

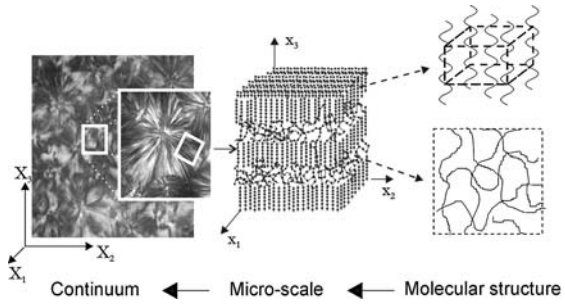


**Fig. 3** The local lamella morphology with indication of crystalline and amorphous phases

subsequently either quenched to room temperature or cooled at 30°C/min to a crystallization temperature of 130°C, held for 30 min and then quenched to room temperature. The later resulted in a well-defined transcrystalline interlayer, Fig. 4a. Processing conditions have a pronounced influence on the evolution of interphases and the morphology of matrix material. Varying the cooling rate changes interphase morphology from almost isotropically oriented spherulitic crystals for low cooling rates to anisotropically oriented crystals along the fibre surface as in Fig. 4b. Obviously, the interphase morphology and morphology of surrounding matrix material together with their mechanical properties influence the residual stresses and, consequently, overall properties of the composite.

Elastic and thermal properties of crystals at the interphase and in the bulk influence value of residual stresses in an encapsulated fibre. The equilibrated structure of molecular crystal and stiffness tensor has been determined using semiempirical quantum mechanical method AM1 [14]. The crystalline unit cell shown in Fig. 5 has lattice parameters $a = c = 1.995$ nm and $b = 2.096$ nm. The resulting stiffness tensor yields following component values

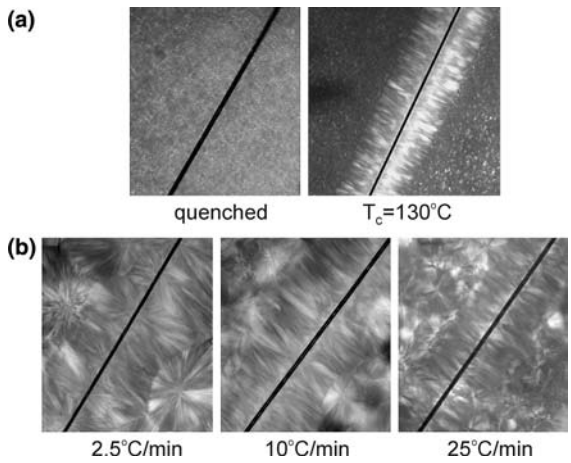


**Fig. 4** Interface morphology under different processing conditions

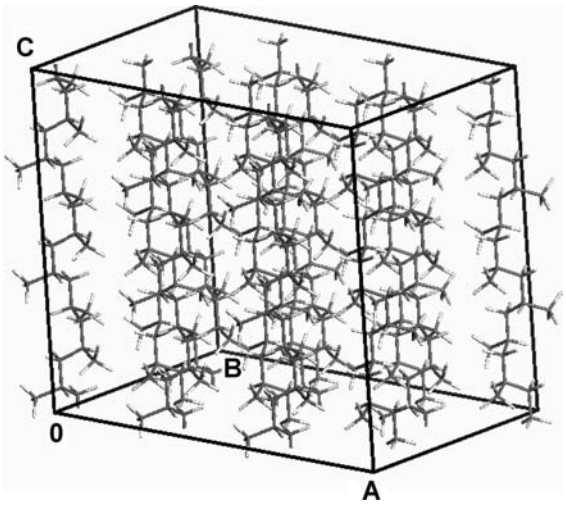


**Fig. 5** Unit cell of polypropylene crystal

$$C^{c}_{ijkl} = \begin{bmatrix} 8.01 & 3.71 & 3.72 & 0.00 & 0.87 & 0.00 \\ 3.71 & 10.85 & 3.89 & 0.00 & -0.38 & 0.00 \\ 3.72 & 3.79 & 41.34 & 0.00 & -0.57 & 0.00 \\ 0.00 & 0.00 & 0.00 & 3.98 & 0.00 & -0.11 \\ 0.87 & -0.38 & -0.57 & 0.00 & 3.13 & 0.00 \\ 0.00 & 0.00 & 0.00 & -0.11 & 0.00 & 2.89 \end{bmatrix} \text{[GPa]} \quad (1)$$

The primitive cell of α-phase iPP crystal has *a*- and *c*-axes three times smaller then the unit cell in Fig. 5 and its coefficients of thermal expansion has been determined by the X-ray diffraction experiments [15].

Interfacial interaction is an extremely complex process due to continuous evolution of interfacial zones during deformation and poses severe interpretation problems going from atomic to continuum descriptions. Polypropylene unit cell has been placed in the close proximity of graphitic plates and subject to energy minimization in order to obtain a stable reference configuration. Two configurations have been investigated having either crystal *c*-axis (Fig. 6a) or crystal *b*-axis (Fig. 6b) perpendicular to the

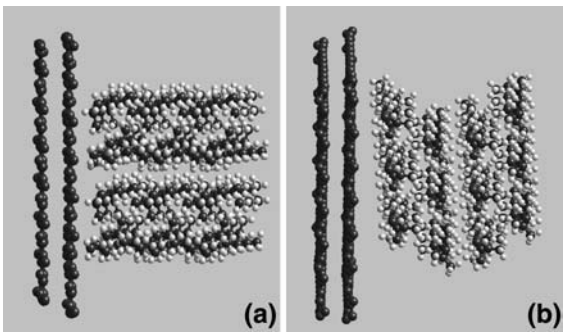


**Fig. 6** Configuration with crystal *c*-axis perpendicular to the graphite plane (**a**) and crystal *b*-axis perpendicular to the graphite plane (**b**)

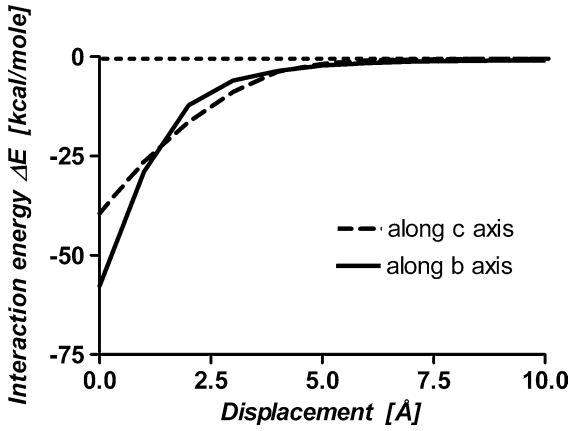


**Fig. 7** Interaction energy for two crystal configurations

graphite plane. The cleavage mode decohesion simulations were performed for both systems. The decohesion process consisted of a number of deformation steps caused by a force applied to the crystal centre of gravity in the direction perpendicular to the graphite planes. The interaction energy has been calculated from the energy difference between the fully cohesive and the complete pullout configuration, which is equal to the work required for moving crystal at distances where crystal does not interact with graphite plates. As it follows from Fig. 7 orienting crystal *b*-axis perpendicular to the graphite plane results in a higher interaction energy and consequently better adhesion than in the case when the crystal *c*-axis makes a right angle with graphite planes. Both configurations seem to be present in the transcrystalline layer as it will follow from the micro-Raman spectroscopy investigations.

Variation of force with the separation distance between crystal and graphite planes is shown in Fig. 8. Once the force reaches maximum value necessary to move the crystal from its equilibrium position then it decreases as the separation distance between crystal and graphite gets larger. It is interesting to notice that the presented force-displacement diagram can be used as an atomic cohesive

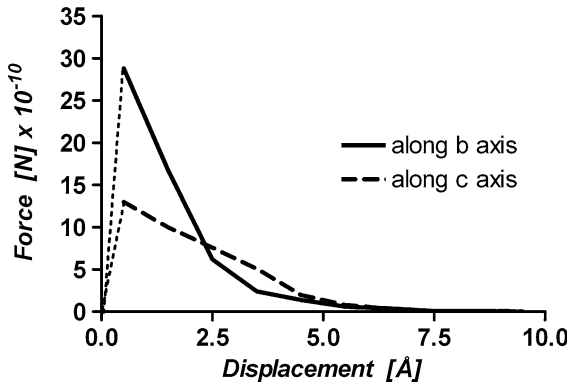


**Fig. 8** Force versus separation distance

zone model in the finite element formulation of the fibre interface problem providing parameter values to cohesive finite elements, which are implemented in many commercially available finite element codes.

An important issue is the development of definitions for continuum quantities that are calculable within a molecular structure. The most frequently used form for the stress at atomic level is based upon the Clausius virial theorem, which determines the stress field applied to the surface of a fixed volume containing interacting particles (atoms) as follows

$$\sigma_{ij}^{\alpha} = \frac{1}{\Omega^{\alpha}}\left(-m^{\alpha}v_i^{\alpha}v_j^{\alpha} + \frac{1}{2}\sum_{\beta}\frac{\partial V}{\partial r^{\alpha\beta}}\frac{r_i^{\alpha\beta}r_j^{\alpha\beta}}{|\mathbf{r}^{\alpha\beta}|}\right), \qquad \frac{\partial V}{\partial \mathbf{r}^{\alpha}} = \mathbf{F}^{\alpha} = \sum_{\beta\neq\alpha}^{N}\mathbf{F}^{\alpha\beta} \tag{2}$$

where $m^{\alpha}$, $\Omega^{\alpha}$ and $v_i^{\alpha}$ are respectively the atom mass, atomic volume and component of the velocity vector, $V$ is the two-body potential acting between two atoms $\alpha$ and $\beta$ separated by the distance $r$, and $\mathbf{F}^{\alpha}$ is the total force acting on atom $\alpha$ from all $\beta$ neighbours. It has been shown that the virial stress cannot be directly related to the classical Cauchy stress and several modifications have been proposed. By using a finite-value and finite-ranged localization function [16] the properties of the atoms are spread out allowing each atom to contribute to a continuum property at the position $\mathbf{r}$. This function has units of inverse volume and is non-zero only in some characteristic volume surrounding the spatial point $\mathbf{r}$ and usually is taken as a radial step function. It is essential to recognize that the stress at the location of an atom depends on the details of the interatomic interactions and the positions of interacting neighbours. Hence, the atomic stress is a nonlocal function of the state of the matter at all points in some vicinity of the reference atom, in contrast to the local stress field used in classical continuum theories. It is also not clear how to use the virial stress formula for cases where the interatomic interactions are described by some multibody potential instead of pair potentials, although some attempts have been made to clarify this problem [17]. Furthermore, atoms in bonded polymeric chains are subject to bending and torsion moments, which are not included in the definition of virial stress. Calculation of interfacial stresses that utilizes the virial theorem or its modifications will not be pursuit her because it seems that the relationship between local displacements of atoms and the strain tensor is not as ambiguous as the concept of atomic stress. Although different strain measures can be formulated all of them rely on the coordinates of atoms. Given a set of atom coordinates the structure of the molecular system can be analyzed by means of the Voronoi tessellation, which

divides space into regions centred on these atoms and defines atomic strain tensor [18]. This issue will not be further pursuit her, nevertheless a simple calculation of adhesion stresses can be made dividing the maximal force that creates separation by the crystal area adjacent to the graphite surface. Then the stress reads 310 and 750 MPa, respectively for configurations (a) and (b) from Fig. 6.

## Interphase level

### Orientation distribution of crystals

Calculation of mechanical anisotropy of the interphase requires the crystal orientation distribution function to be determined. Raman microspectroscopy can be applied to study the crystalline orientation distribution function, which is related to the Raman scattering intensity in a polarized light experiment [19]. It follows from the relations between Raman scattering intensity and Legendre coefficients of the crystal orientation distribution function that measurements on three orthogonal planes must be made in order to determine the moments of the orientation distribution, Fig. 9. The transcrystallized and subsequently quenched sample has been carefully polished to obtain three perpendicular free surfaces on which Raman spectra of the six different polarizations could be acquired. The

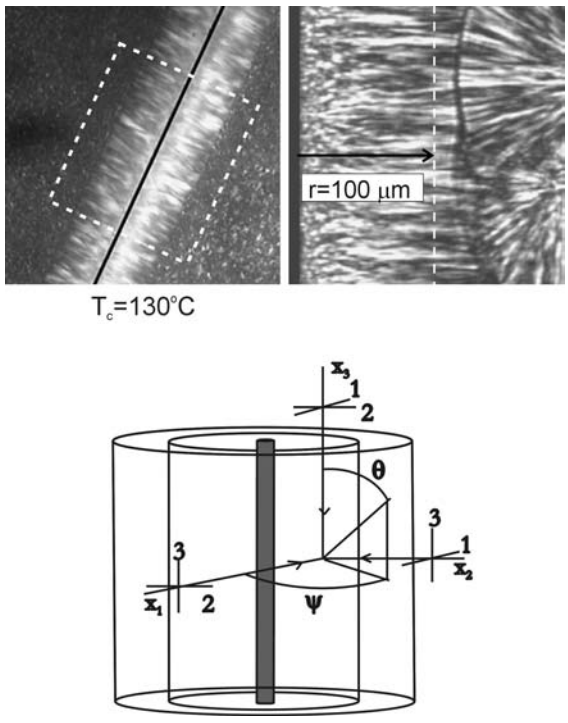


**Fig. 9** Measurement of crystal orientation on three orthogonal planes in the transcrystalline layer

orientation distribution function of *c*-axis of crystals $N(\theta,\psi,\phi)$ can be expressed as

$$N(\theta,\psi,\phi) = \sum_{l=0,2,4} \sum_{m=-l} \sum_{n=-l} W^{lmn} Z^{lmn}(\cos\theta) \mathrm{e}^{-im\psi} \mathrm{e}^{-in\phi} \tag{3}$$

where $Z^{lmn}$ are generelized Legendre functions and $W^{lmn}$ the expansion coefficients. Since the orientation of crystal c-axis is axially symmetric along the fibre axis, the calculation of the orientation distribution function is independent of the angle $\phi$. It follows from the theory of Raman scattering that the scattering intensity can be related to the expansion coefficients of the orientation distribution function $N(\theta,\psi)$. Form six intensity measurements on three orthogonal planes six expansion coefficients can be determined yielding the orientation distribution function of crystals in the transcrystalline phase, Fig. 10. It can be seen that there is a preferred *c*-axis orientations at angles, where the orientation distribution function attains its local maxima.

### Aggregate model

The lamellae morphology of semicrystalline matrix material can be described by an aggregation model containing crystalline (c), amorphous (a) and defect (b) regions. The later exists within the crystal region. Chains of the defect region are not packed in a lattice but their motion is constrained by the surrounding lattice. In principle, the behaviour of the defect region is different from the amorphous region. It has been also observed that the volume fraction of defect region is proportional to the volume fraction of the crystalline region which indicates a correlation between (c) and (b) phases. The three-phase structure of the aggregate model is shown in Fig. 11.

The parameters $\chi^1$ and $\chi^2$ are defined in terms of the volume fractions of the phases

$$\begin{aligned} \chi^1 &= \chi^b/(1-\chi^a) \\ \chi^2 &= \chi^a \end{aligned} \tag{4}$$

where $\chi^b = 0.83\chi^c$ *and* $\chi^a = 1-\chi^c-\chi^b$. The volume fraction of phases has been experimentally determined using Raman microspectroscopy [20]. Local response matrices of stiffness $C_{ijkl}$, compliance $S_{ijkl}$ and thermal expansion $\alpha_{ij}$ are derived by assuming constant stress or constant strain within each phase as follows [21]

- constant stress

$$\begin{aligned} &\varepsilon = \varepsilon_a + \varepsilon_b, \varepsilon_b = \varepsilon_c \\ &\sigma = \sigma_a = \sigma_b + \sigma_c \end{aligned} \tag{5}$$

gives

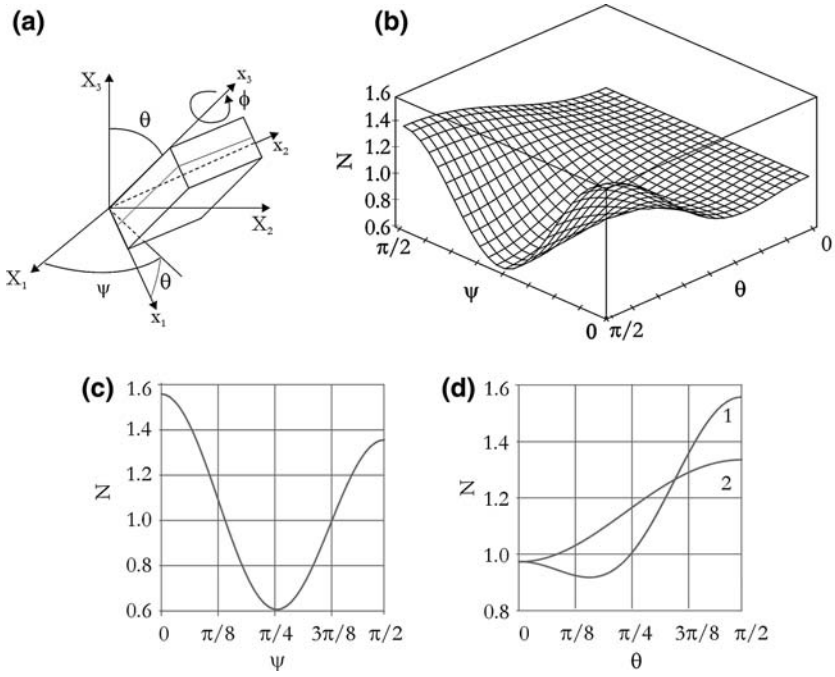


**Fig. 10** Euler angles (**a**); orientation distribution of *c*-axis $N(\theta, \psi)$ (**b**); orientation distribution in plane $x_1$-$x_2$ (**c**); orientation distribution (1) in plane $x_1$-$x_3$ and (2) in plane $x_2$-$x_3$ (**d**)

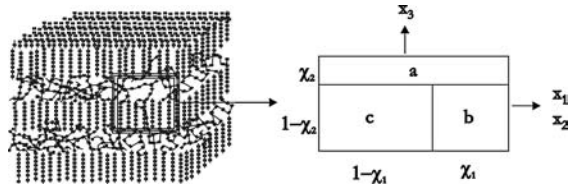


**Fig. 11** Representative volume element of the three-phase aggregate model

$$S_{ijkl} = (C^b_{ijkl}\chi_1 + C^c_{ijkl}(1-\chi_1))^{-1}(1-\chi_2) + S^a_{ijkl}\chi_2$$
$$\alpha_{ij} = \chi_2\alpha^a + \frac{(1-\chi_2)(\alpha^c_{ij}C^c_{ijij}(1-\chi_1) + \alpha^b C^b_{ijij}\chi_1)}{C^c_{ijij}(1-\chi^c) + C^b_{ijij}\chi_1} \quad (6)$$

- constant strain

$$\varepsilon = \varepsilon_a = \varepsilon_b + \varepsilon_c$$
$$\sigma = \sigma_a + \sigma_b, \sigma_b = \sigma_c \quad (7)$$

yields

$$C_{ijkl} = (S^b_{ijkl}\chi_1 + S^c_{ijkl}(1-\chi_1))^{-1}(1-\chi_2) + C^a_{ijkl}\chi_2$$
$$\alpha_{ij} = \frac{(\alpha^a\chi_1 + \alpha^c_{ij}(1-\chi_1))(1-\chi_2) + (S^b_{ijij}\chi_1 + S^c_{ijij}(1-\chi_1))\alpha^a C^a_{ijij}\chi_2}{(1-\chi_2) + (S^b_{ijij}\chi_1 + S^c_{ijij}(1-\chi_1))C^a_{ijij}\chi_2} \quad (8)$$

The effective properties of the semicrystalline matrix material are determined by spatial averaging over the representative volume element. Formally it means that any property $P$ can be spatially averaged with the orientation distribution function $N$ as

$$<P_{ijkl}> = \int_0^{2\pi}\int_0^{2\pi}\int_0^{\pi} N(\theta,\psi,\phi)a_{ip}a_{jq}a_{kr}a_{ls} \times P_{pqrs}(p_i,d_i)\sin\theta \mathrm{d}\theta\mathrm{d}\psi\mathrm{d}\phi \quad (9)$$

where $a_{ij}$ is the transformation matrix having Euler angles as components, $p_i$ are the properties of the individual phases and $d_i$ is a set of morphological descriptors coupled with phases properties.

Thus the averaged stiffness, compliance and thermal expansion properties of the aggregate model can be written with Eq. 9 as a template after substitution Eq. 3 into it

$$\langle C_{ijkl}\rangle = \sum_{1=0,2,4}\sum_{m=-1}^{l}\sum_{n=-1}^{l} W^{lmn} I^{Clmn}_{ijklpqrs} C_{pqrs}(C^{a,b,c}_{pqrs}, S^{a,b,c}_{pqrs}, \chi^{a,b,c})$$
$$\langle S_{ijkl}\rangle = \sum_{1=0,2,4}\sum_{m=-1}^{l}\sum_{n=1}^{l} W^{lmn} I^{S,lmn}_{ijklpqrs} S_{pqrs}(C^{a,b,c}_{pqrs}, S^{a,b,c}_{pqrs,}\chi^{a,b,c})$$
$$\langle \alpha_{ij}\rangle = \sum_{1=0,2}\sum_{m=-1}^{l}\sum_{n=-1}^{l} W^{lmn} I^{\alpha,lmn}_{iijpq}\alpha_{pq}(\alpha^{a,b,c}_{pq}, C^{a,b,c}_{pqrs,}S^{a,b,c}_{pqrs}, \chi^{a,b,c}) \quad (10)$$

where $C^{a,b,c}_{pqrs}$, $S^{a,b,c}_{pqrs}$ and $\alpha^{a,b,c}_{pq}$ are the properties of phases *a, b* and *c* of the aggregate model, $C_{pqrs}$, $S_{pqrs}$ and $\alpha_{pq}$ are the solutions from Eqs. 6 and 8, $I^{C,lmn}_{ijklpqrs}$, $I^{S,lmn}_{ijklpqrs}$, $I^{\alpha,lmn}_{iijpq}$ are the expression containing averaging integrals and Legendre functions from Eqs. 3 and 9, and finally $\chi^{a,b,c}$, $W^{lmn}$ defines crystallinity and crystalline orientation.

Amorphous phases

The defect phase (b) remains elastic due to constrain from the surrounding crystalline lattice, whereas amorphous phase (a) exhibits viscoelastic behaviour. It is further assumed that the instantaneous elastic response of phases (a) and (b) are equal. A relaxation function for phase (a) takes the form

$$E^a(T,t) = E^{a0}(T) + C \cdot b^a(T)(a^a t)^n \tag{11}$$

where $E^{a0}$ is the instantaneous modulus, $a^a$ and $b^a$ are respectively horizontal and vertical shift factors, and $C$, $n$ are constants. These parameters were determined by fitting the aggregate model to properties of the bulk polymer, using known volume fraction of phases [20]. The fitting procedure was accomplished by minimization of the square of the difference between the aggregate model and measured relaxation modulus at different temperature

$$\min\left|(E_{iPP}(T_i,t) - \langle S_{kkkk}\rangle^{-1}(T_i,t))^2; (E^{a0}, C, b^a, a^a, n)\right| \tag{12}$$

where $\langle S_{kkkk}\rangle^{-1} = \langle S_{1111}\rangle^{-1} = \langle S_{2222}\rangle^{-1} = \langle S_{3333}\rangle^{-1}$ (for $W^{lmn}$=0,1≥2), and $E_{iPP}$ is the measured relaxation modulus. Figure 12 shows prediction of the aggregate model compared to the experimental data for iPP polymer. The constants $C$ and $n$ read values –419 and 0.0095, respectively. The temperature dependent parameters of the relaxation function are shown in Fig. 13 together with the master curve for the amorphous matrix.

## Fibre level

Non-isothermal crystallization

Crystallization kinetics of semicrystalline polymers is highly dependent on the cooling rate through the temperature range of crystallization. It is of practical interest to study the non-isothermal crystallization kinetics as the processing of thermoplastic based materials involves cooling from the melt through the temperature range of crystallization. Crystallinity affects dilatational behaviour and mechanical properties of the polymer and a relation between cooling rate and crystallization kinetics may lead to improved understanding of the evolution of residual stresses in polymer based materials. Crystallization is composed of primary and secondary crystallization stages. Primary crystallization is characterized by nucleation and growth of spherulitic domains. When spherulites impinge the growth is terminated and the secondary intraspherulitic crystallization commences resulting in densification of the matrix. Figure 14 shows images of progressing crystallization and schematics of the crystallization within point $P$. The degree of conversion between polymer melt and solid crystallites can be written as

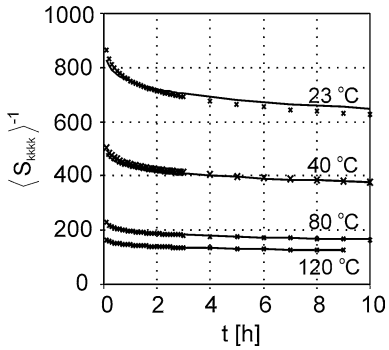


**Fig. 12** Fit of the aggregate model to viscoelastic data

$$C(T) = \frac{\chi^c(T)}{\chi^{c\infty}} \tag{13}$$

where $\chi^c(T)$ is the degree of crystallinity at temperature $T$ and $\chi^{c\infty}$ is the degree of crystallinity reach at the end of cooling. Derivation of the expressions for the degree of conversion for both primary and secondary crystallization processes as well as corresponding measurements of the degree of crystallinity using optical and Raman microscopy allows to determine the evolution of matrix morphology during cooling process [13, 22]. Crystallization process in a bulk such as in Fig. 14 is homogeneous as opposed to the heterogeneous crystallization, which may be trigged by a presence of inclusions and their surfaces. Heterogeneous crystallization is characterized by higher nucleation temperature and nucleation density on the surfaces, resulting in constrained growth and the formation of an anisotropic layer. The evolution of crystalline phase during cooling under either homogeneous or heterogeneous conditions can be quantified by the same type of equation with parameters having obviously distinct values for specific condition. The total crystallinity can be described in terms of a convolution integral

$$\chi^c(T) = C^I(T)\chi^{cI\,\infty} - \frac{\chi^{cII\,\infty}}{R}\int_0^T C^{II}(\tau)\frac{\mathrm{d}}{\mathrm{d}\tau}[C^I(T-\tau)]\mathrm{d}\tau \tag{14}$$

where $C^I$ and $C^{II}$ are the conversion rates for primary and secondary crystallization process, respectively and $R$ is cooling rate. Parameters for the homogeneous crystallization process were determined in [22]. Figure 15a shows the relative contribution from the primary and secondary process to the degree of conversion at cooling temperature of 25 °C/min. The secondary process amounts to a substantial

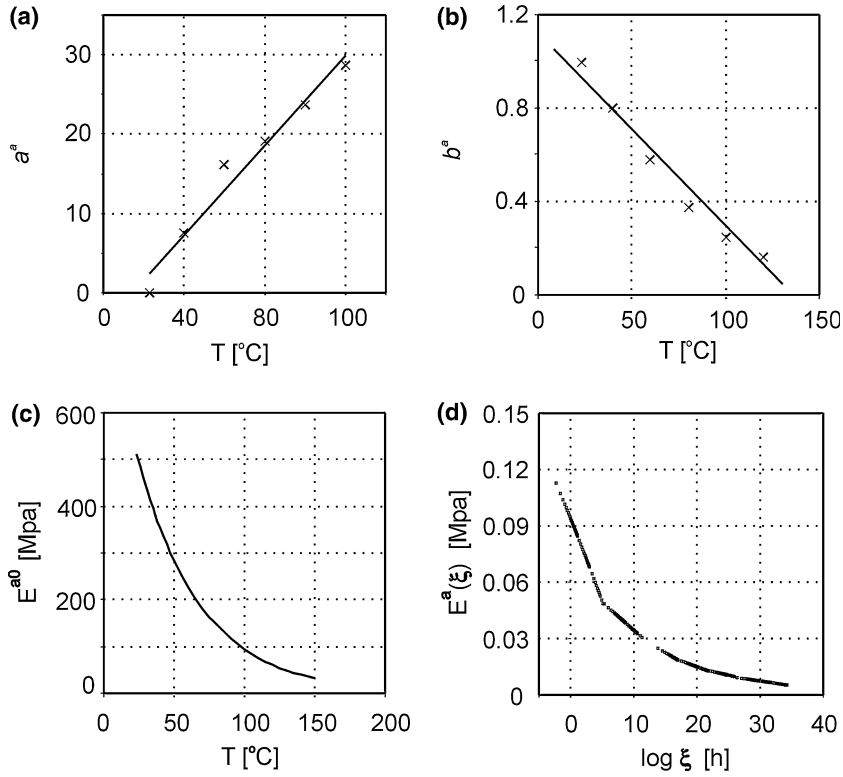


**Fig. 13** Horizontal (**a**) and vertical shifts (**b**), instantaneous elastic modulus (**c**) and the master curve for amorphous phase (**d**)

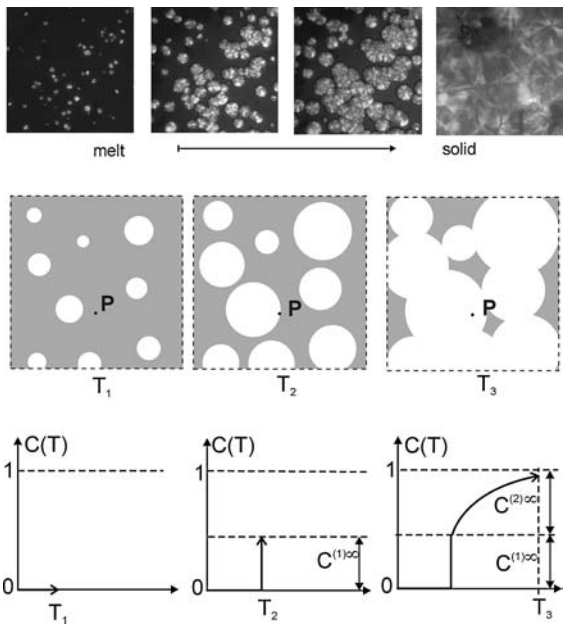


**Fig. 14** Illustration of primary and secondary crystallization

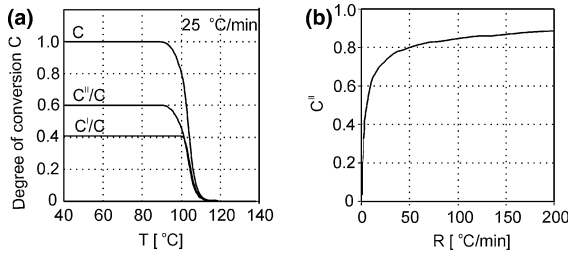


**Fig. 15** Contribution from the primary and secondary crystallization to the degree of conversion (**a**) and contribution of secondary crystallization as a function of cooling rate (**b**)

part of the total crystallization process at this particular cooling rate. The contribution from the secondary process increases with increasing cooling rate, Fig. 15b. The presence of a substrate such as fibre may influence the nucleation kinetics by providing sites for heterogeneous nucleation. The presence of the substrate affects the nucleation kinetics by lowering the energy barrier thus increasing the nucleation temperature and nucleation rate, whereas growth rate and subsequent secondary crystallization are the same as for the bulk crystallization. The case of heterogeneous crystallization is shown in Fig. 16. The degree of conversion from melt to crystallized state is governed by both heterogeneous crystallization and homogeneous crystallization, which corresponds to the creation of transcrystalline layer and spherulitic structure, respectively, as in Fig. 16a. When the volume fraction of fibres and the heterogeneous nucleation density are high, the crystallization of the matrix develops predominantly in a form of transcrystallinity, Fig. 16b. The degree of conversion by the primary process, in terms of the inter-fibre distance $r^m$ defining the fibre volume fraction $V = (r^f)^2/(r^m)^2$ is given by

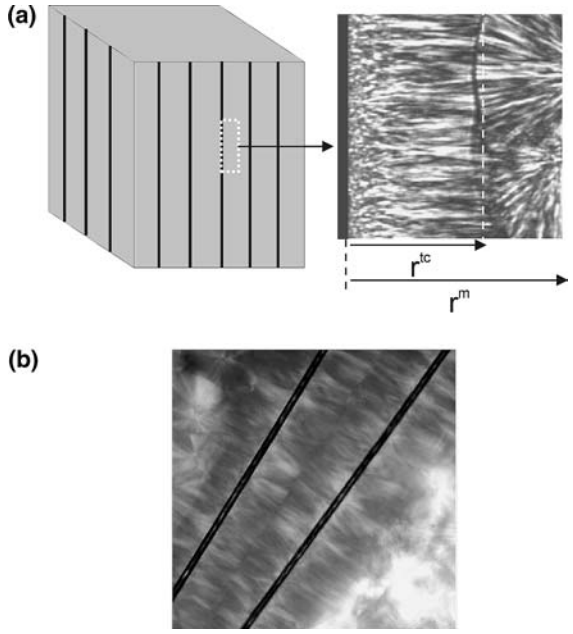


**Fig. 16** Heterogeneous and homogeneous crystallization (**a**) and completely heterogeneous morphology of the matrix (**b**)

$$C^I_{\text{heter}} = \frac{(r^{tc})^2 - (r^f)^2}{1-V} + \frac{(r^m)^2 - (r^{tc})^2}{1-V} C^I_{\text{hom}} \tag{15}$$

and $C^I_{\text{hom}}$ is the degree of conversion by the primary process under homogeneous crystallization. As the secondary heterogeneous process is independent of the interfacial energy thus equal to the secondary process for bulk crystallization, the degree of crystallinity for heterogeneous process again takes a form as in Eq. 14. Figure 17a shows the influence of the crystallization temperature for homogeneous and heterogeneous crystallization. The heterogeneous nucleation occurs at a higher temperature than in the bulk. However, increasing cooling rate, the difference decreases

## Residual stresses

When spherulites are heterogeneously nucleated, a solidified interlayer is instantly formed around the fibre. Modelling of the transcrystalline growth is accomplished by a

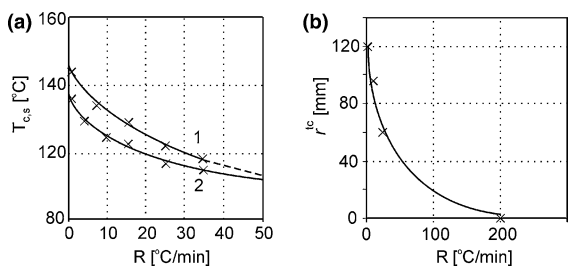


**Fig. 17** Nucleation/crystallization temperature for heterogeneous (1) and homogeneous (2) crystallization (**a**) and thickness of transcrystalline layer as a function of cooling rate (**b**)

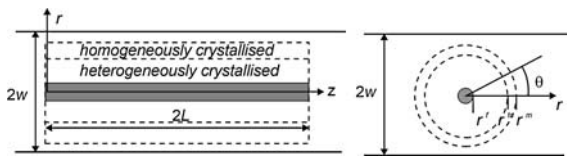


**Fig. 18** Three component model for a single fibre composite

composite model consisting of fibre, transcrystalline interlayer and bulk matrix, Fig. 18. The elastic solution for the composite model with an anisotropic interlayer can be solved based upon shear-lag assumptions [21, 23]. In the present case however, the time and temperature dependent solution is needed. A direct viscoelastic solution of the above-mentioned problem involves an inversion of the Laplace transform of corresponding hereditary integral, which cannot be solved exactly. Instead, a quasi-elastic approach has been used that utilizes the elastic solution as follows [24]

$$\sigma(t) = \int_0^{\xi} \sigma^e\left(\left\langle C^m_{ijkl}(\xi - \xi')\right\rangle, \left\langle \alpha^m_{ij}\right\rangle\right) \frac{\mathrm{d}T}{\mathrm{d}\xi'} \mathrm{d}\xi' \tag{16}$$

where $\sigma^e$ is the elastic solution for the embedded single fibre subject to a unit step change in temperature and $\langle C^m_{ijkl} \rangle$, $\langle \alpha^{\ m}_{ij} \rangle$ are the properties of the matrix determined by the aggregate model. The hereditary integral (16) is solved by the time incremental approach together with a simultaneous solution of the convolution integral determining evolution of crystallinity (14). Thermal stress evolution during cooling is shown in Fig. 19 where the experimental results are compared to the predictions of the aggregate model. The distribution of thermal stresses along fibre axis is presented in Fig. 20 for cooling rates differing by an order of magnitude. As it follows from micrographs taken in room temperature the nucleation density of transcrystalline layer obtained with cooling rate 2.5 °C/min is low and its morphology is different than in the samples with higher cooling rate. The degree of anisotropy is quite small in samples cooled slowly and therefore, the isotropic aggregate model is better suited in those cases

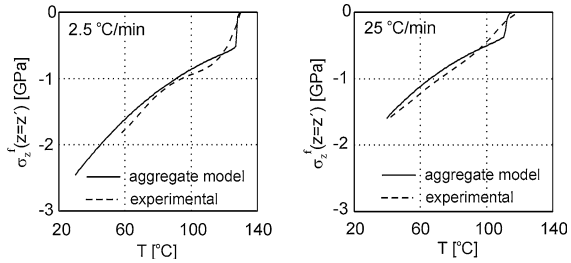


**Fig. 19** Thermal stress evolution in fibre at different cooling rates

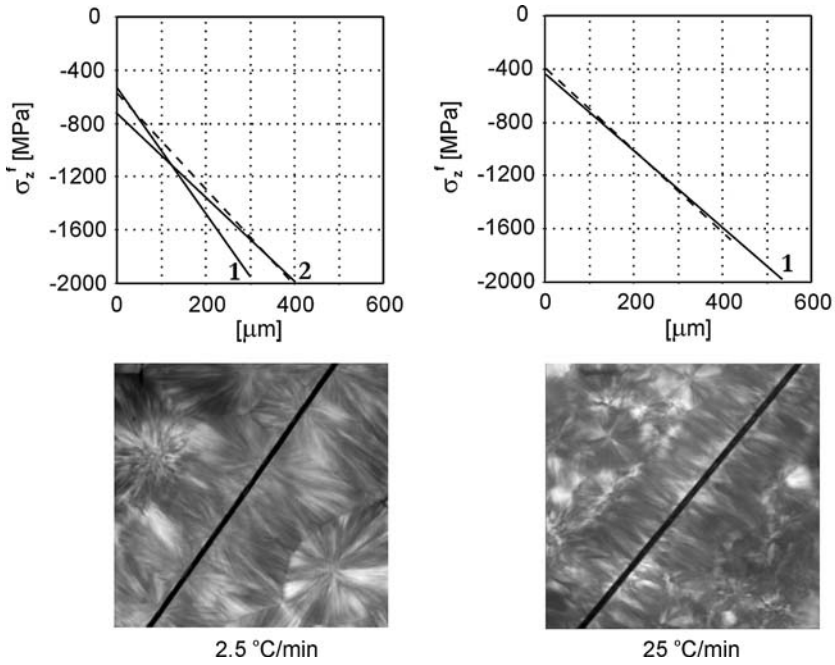


**Fig. 20** Thermal stress distribution along fibre axis: dashed line—experimental data, solid line—aggregate model with anisotropic (1) and isotropic solution (2)

## Continuum level

### Constitutive model

A multiphase material is by definition heterogeneous and its local properties vary spatially. If the material is statistically homogeneous, which means that the local material properties are constant when averaged over a representative volume element and then it is possible to replace the real disordered material by a homogeneous one where the local material properties are the averages over the representative volume element in the real material. Estimation of those averages presents a fundamental issue for different effective medium theories [12, 25–28]. Calculation of effective creep properties of short fibre composites is based upon derivations presented in [29–31]. The methodology utilized a modified Mori–Tanaka approach [32] and allows calculating effective creep properties including imperfect interfaces between the fibres and matrix material as well as taking into account arbitrary orientation distribution of fibres. The non-perfect bonding is modelled as a spring layer of vanishing thickness. If $S$ and $n_i$ denotes the interface and its unit normal then the tractions must vanish at the interface

$$\Delta\sigma_{ij}n_j = \left[\sigma_{ij}(\mathbf{x})\big|_{S^+} - \sigma_{ij}(\mathbf{x})\big|_{S-}\right]n_j = 0 \tag{17}$$

where $S^+$ and $S^-$ denote approaching the interface from outside or inside of the inclusion and the displacement jump $\Delta u_i(\mathbf{x})$ is

$$\Delta u_i = \lfloor u_i(\mathbf{x})|_{S^+} - u_i(\mathbf{x})|_{S-} \rfloor = \eta_{ij}\sigma_{jk}n_k \tag{18}$$

with the interface compliance $\eta_{ij} = \alpha\ \delta_{ij} + (\beta - \alpha)n_i\ n_j$. Parameters $\alpha$ and $\beta$ represent the compliance in the tangential and normal direction of the interface, respectively. Setting $\beta = 0$ and $\alpha$ to a small value will represent softening of the interface. The incremental formulation of the creep process contains the stiffness tensor for the matrix material. This tensor can be calculated with the aggregate model as explained in the previous chapter, however in the present paper properties of the matrix material are taken from [31].

### Fibre orientation distribution

An important aspect of microstructure's morphology is shape and orientation size of reinforcing constituents. In the case of short fibre composites the fibres are considered as being circularly cylindrical with a finite length. The distribution of fibres' diameters may be easily inferred from planar sections of the material, where the intersections with fibres appear in a form of elliptical profiles. The minor axis of an ellipse represents the fibre diameter. A rather different situation arises when one wants to determine length distribution of short fibres embedded in the matrix material. The simplest way to extract fibre lengths is to burn off the matrix material and then perform length measurements in an image analyzer. However, the pyrolysis technique by itself may cause fibres' fragmentation, and its usefulness depends upon a particular combination

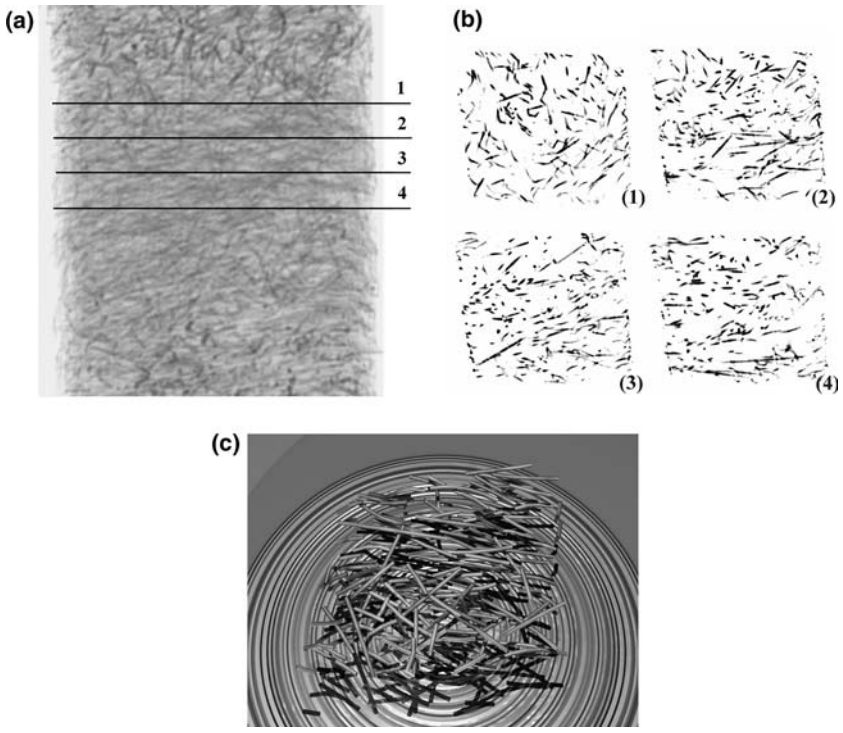


**Fig. 21** Transmission micrograph of short fibre composite (**a**), reconstructed 2D sections (**b**) and 3D configuration if fibres (**c**)

of constituent phases. Also measurements of fibre lengths made before processing are doubtful, as some processing techniques, like for example an injection molding, may result in fibre breaking. The length distribution of fibres can be assessed using stereological approaches [33] or X-ray microtomography [34–36], which allows to disclose fibre orientation distribution as shown in Fig. 21. The orientation distribution function $g(\theta, \psi)$ describes a number of fibre directions that cross a unit sphere surface in terms of Euler angles as in Fig. 10a. The distribution function does not depend on the rotation angle $\phi$ and for injection moulded samples the fibre orientation is uniformly distributed with respect to $\psi$, thus the distribution is related only to the angle $\theta$ and can be described in the following form

$$g(\theta) = \frac{\sin(\theta)^{2P-1}\cos(\theta)^{2Q-1}}{\int_{\theta_a}^{\theta_b}\sin(\theta)^{2P-1}\cos(\theta)^{2Q-1}\mathrm{d}\theta} \tag{19}$$

where $\theta^a$ and $\theta^b$ are the upper and lower limits of the angle $\theta$ that is present in the distribution and $P \geq 0.5$, $Q \geq 0.5$. The orientation distribution of fibres is taken into account in the procedure leading to the determination of overall creep deformation by averaging the eigenstrains overall directions present in the representative volume element [29–31]. By appropriately adjusting parameters of the distribution function it is possible to describe both narrow and more smeared out distributions along preferred directions as shown in Fig. 22. The results of calculations of creep strains are shown in Figs. 23 and 24. The applied uniaxial stress is 4 MPa and softening parameter $\alpha = 8\ \mathrm{e}^{-6}\ \mathrm{MPa}^{-1}$. As expected the creep strains in samples with preferred orientation along the loading direction are significantly lower that for samples having fibres gathering around 45°. Furthermore, there are more differences between perfect and imperfect samples when the distribution is wider and the preferred orientation is along 0° direction. The width of

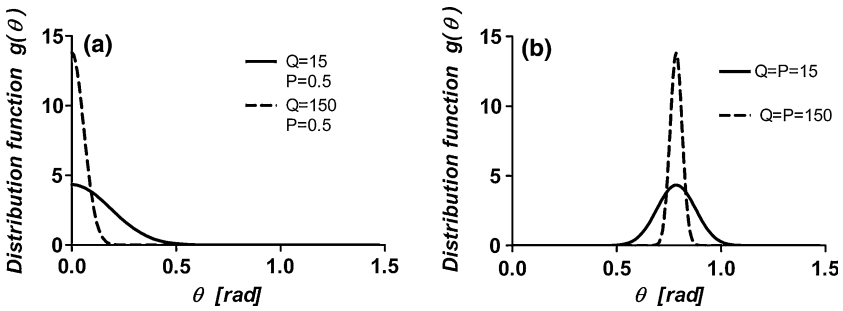


**Fig. 22** Orientation distribution functions for preferred orientation along 0° direction (**a**) and 45° direction (**b**)

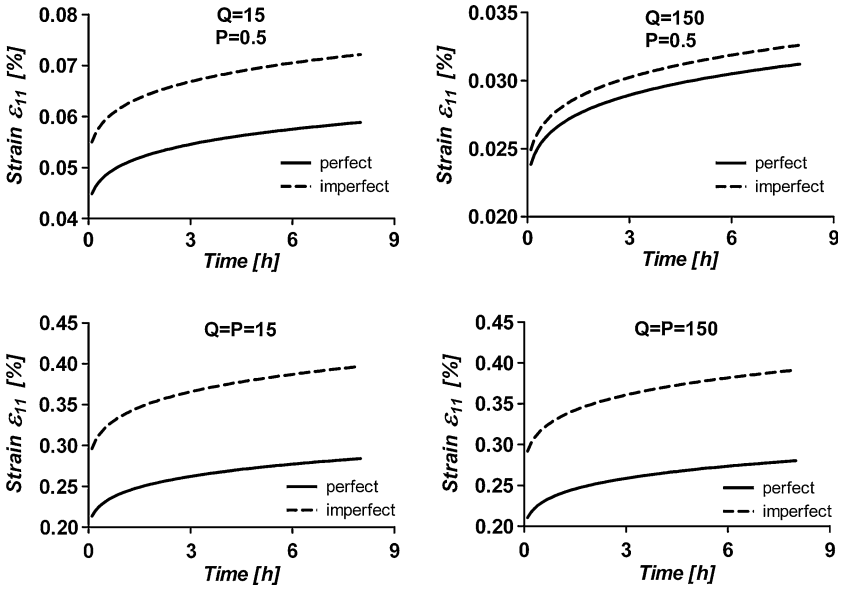


**Fig. 23** Creep strains in uniaxial tension

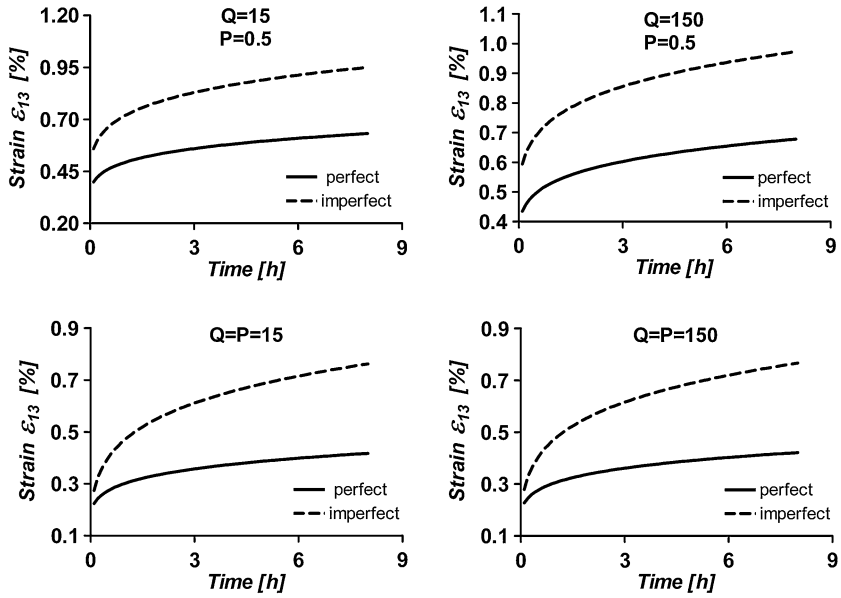


**Fig. 24** Creep strains in uniaxial shear

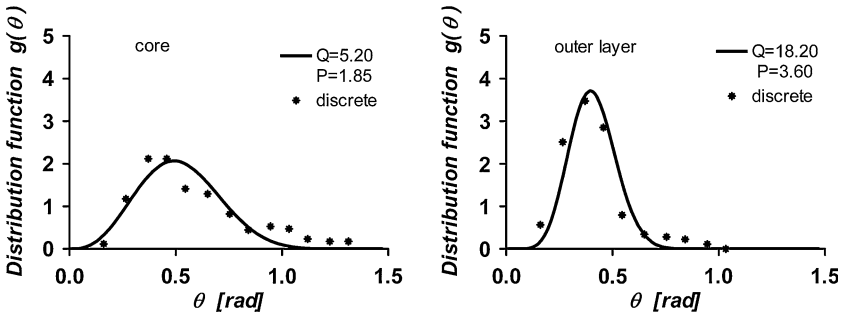


**Fig. 25** Orientation distribution function for samples processed with low injection velocity

the distribution does not influence the creep response when the fibres are oriented along 45° independently whether they are perfectly or imperfectly bonded. The corresponding conclusions can be drawn for the creep strains under shear loading conditions. It is interesting to notice that the creep strains in 0° and 45° samples loaded in uniaxial tension differ

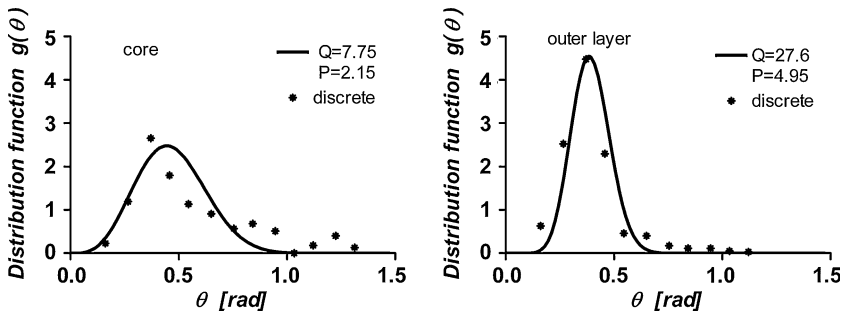


**Fig. 26** Orientation distribution function for samples processed with high injection velocity

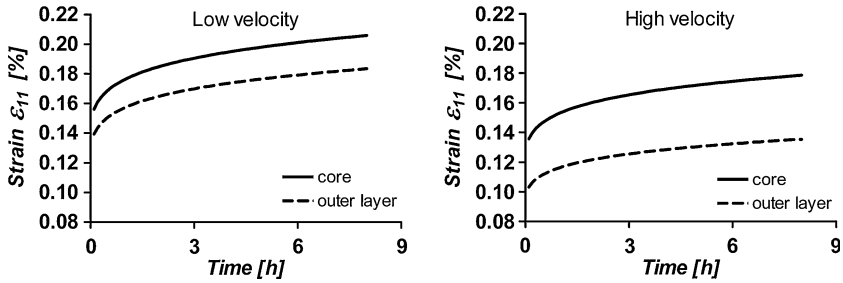


**Fig. 27** Creep strains in uniaxial tension for both injection velocities

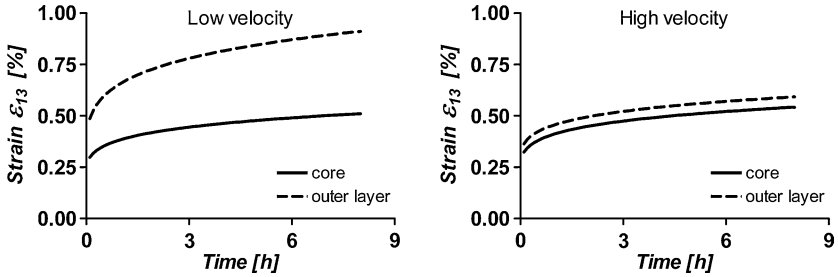


**Fig. 28** Creep strains in uniaxial shear for both injection moulding velocities

by one order of magnitude whereas in uniaxial shear this difference is of the same magnitude as strains themselves.

The orientation distribution of fibres in samples prepared by an injection moulding technique has been measured in the core region of the samples and in the outer skin layer. The batches were prepared by performing injection moulding with a low and high velocity. The experimental data has been approximated by the distribution function $g(\theta)$ as in Eq. 19. As it follows from Figs. 25 and 26 the distribution of fibres is narrower in samples prepared with high injection velocity. Furthermore, the fibres in the skin a better aligned as compared to the fibres in the core region. This is a result of a constraint from the mould wall. The same creep strain analysis has been conducted as before. The results are shown in Figs. 27 and 28. Better alignment of fibres caused by high injection velocity results in smaller creep strains as compared to low velocity samples. The creep resistance is pronouncedly higher in uniaxial tension than in uniaxial shear and the creep strain level seems to be velocity independent for the core and skin regions.

## Conclusion

The methodology for bridging the gap between different length scales has been presented and illustrated for the determination of the overall creep behaviour of short fibre reinforced composite material. What is clear is the importance of macroscopic methods: elasticity and viscoelasticity theory and their generalizations. Furthermore, the manufacturing conditions should be accounted for at different scale levels. Obviously, these approaches are too simple to be applied at the atomic scale. But the continuum theories provide a limit for atomic treatments for regions of larger sizes, and they provide a tool for embedding sophisticated atomistic or molecular subsystems within a representation of its real environment.

**Acknowledgement** The authors would like sincerely to acknowledge Dr. A.S. Nielsen for providing some numerical data and micrographs contained in this research work.

## References

1. Zhou M, McDowell DL (2002) Phil Mag A 82:2547
2. Chen Y, Lee JD (2003) Physica A 322:359
3. Chen Y, Lee JD, Eskandrian A (2003) Acta Mech 161:81
4. Picu RC (2002) J Mech Phys Sol 50:1923
5. Liu B, Huang Y, Jiang H, Qu S, Hwang KC (2004) Comput Methods Appl Mech Eng 193:1849
6. Tadmor EB, Phillips R, Ortiz M (1996) Langmuir 12:4529
7. Knap J, Ortiz M (2001) J Mech Phys Sol 49:1899
8. Miller RE, Tadmor EB (2002) J Comp Aided Mat Des 9:203
9. Rudd RE, Broughton JQ (2000) Phys Stat Solidi B 217:251
10. Wagner GJ, Liu WK (2003) J Comp Phys 190:249
11. Mura T (1987) Micromechanics of defects in solids. Kluwer, Dordrecht
12. Nemat-Nasser S, Hori M (1993) Micromechanics: overall properties of heterogeneous materials. North-Holland, Amsterdam
13. Nielsen AS, Pyrz R (2003) J Mat Sci 38:597
14. Dewar MJS, Jie C (1987) Organometallics 6:1486
15. Isasi IR, Alamo RG, Mandelkern L (1997) J Polym Sci Polym Phys 35:2945
16. Hardy RJ (1982) J Chem Phys 76:622
17. Delph TJ (2005) Modell Simul Mater Sci Eng 13:585
18. Pyrz R (2005) In: Sadowski T (ed) Proceedings of the IUTAM symposium on multiscale modelling of damage and fracture process in composite materials, Kazimierz Dolny, Kluwer, Dordrecht, in print
19. Bower DI, Maddams WF (1992) The vibrational spectroscopy of polymers. Cambridge University Press
20. Nielsen AS, Batchelder DN, Pyrz R (2002) Polymer 43:2671
21. Nielsen AS, Micromechanical modeling of thermal stresses in polymer matrix composites based on Raman microscopy, Ph.D. thesis, Special Report No. 43, Aalborg University, May 2000
22. Nielsen AS and Pyrz R, Report, August 2001, Institute of Mechanical Engineering, Aalborg University, ISBN 87-89206-54-1
23. Budiansky B, Hutchinson JW, Evans AG (1986) J Mech Phys Solids 34:167
24. Schapery RA (1967) J Comp Mat 1:228
25. Aboudi J (1991) Mechanics of composite materials. Elsevier, Amsterdam
26. Dvorak GJ (1992) Proc R Soc Lond A 437(8):311
27. Zhu ZG, Weng GJ (1990) Mech Mater 9:93
28. Takao Y, Chou TW, Taya M (1982) J Appl Mech 49:536
29. Schjødt-Thomsen J, Pyrz R (2000) Mech Mater 32:349
30. Schjødt-Thomsen J, Pyrz R (2001) Comp Sci Techn 61:697
31. Schjødt-Thomsen J, Pyrz R (2002) Key Engng Mater 221–222:267
32. Mori T, Tanaka K (1973) Acta Metall 21:571
33. From PS, Pyrz R (1999) Sci Engng Comp Mater 8:143
34. Pyrz R (2000) In: Wojnar L, Rozniatowski K (eds) Proceeding of 6th International conference on stereology and image analysis in materials science, Cracow, Mes-Print, Cracow, 59
35. Nygaard JV, Pyrz R (2003) Cellular Polym 22:347
36. Pyrz R, Nygaard JV, In: d. Bruno et al. (eds) Proceeding of the International Conference Composites in Structures, Cosenza, September 2003, Editoriale-Bios, Cosenza, 189